# ANALYSIS OF FLAT FIELDS IN EDGE ILLUMINATION PHASE CONTRAST IMAGING

*Ben Huyge, Jonathan Sanctorum, Nathanaël Six, Jan De Beenhouwer, Jan Sijbers*

imec-Vision Lab, Department of Physics, University of Antwerp,
Universiteitsplein 1, 2610 Antwerp, Belgium

## ABSTRACT

One of the most commonly used correction methods in X-ray imaging is flat field correction, which corrects for systematic inconsistencies, such as differences in detector pixel response. In conventional X-ray imaging, flat fields are acquired by exposing the detector without any object in the X-ray beam. However, in edge illumination X-ray CT, which is an emerging phase contrast imaging technique, two masks are used to measure the refraction of the X-rays. These masks remain in place while the flat fields are acquired and thus influence the intensity of the flat fields. This influence is studied theoretically and validated experimentally using Monte Carlo simulations of an edge illumination experiment in GATE.

***Index Terms*—** Flat fields, white fields, edge illumination, phase contrast CT, flat field correction

## 1. INTRODUCTION

Conventional X-ray images show contrast based on local differences in attenuation of the beam passing through the object. This attenuation contrast can easily distinguish high-absorbing materials from low-absorbing materials (e.g., bone and muscle), but attenuation contrast between different soft tissues (e.g., muscle and tumor) is, however, often rather weak. On the other hand, the difference in phase shift of the X-ray wave front is a considerably stronger effect for these materials [1]. X-ray phase contrast imaging (XPCI) techniques are capable of measuring such phase shifts and their application in lab-based X-ray imaging has been emerging over the past decade [2]. Current lab-based XPCI methods can be divided into interferometric methods, like grating interferometry, and non-interferometric methods, such as edge illumination (EI).

Apart from the phase, EI-XPCI also yields the conventional attenuation image and a so-called dark field image [3]. The latter is a measure of the amount of small angle scattering in the phantom. The phase is retrieved via the refraction angle of the X-rays, measured through the use of two masks with parallel aperture slits. The sample mask divides the incoming X-ray beam into separate smaller beams (beamlets) and the detector mask covers the edges of the pixel columns, as shown in Fig. 1. EI-XPCI is a non-interferometric technique, as the apertures sizes are about an order of magnitude larger compared to interferometric methods. This allows the use of relatively simple geometric ray optics to explain EI-XPCI.

Similar to conventional, attenuation based X-ray imaging, EI-XPCI requires flat field correction to normalize the acquired X-ray projection images. This correction eliminates systematic inconsistencies in the image (e.g., a difference in detector element response or inhomogeneity in the X-ray beam) [4]. In conventional X-ray imaging, flat fields are obtained by exposing the detector without any object in the X-ray beam. The flat field correction is then performed by dividing the acquired projections by the flat field. The flat fields in EI-XPCI differ from those of conventional X-ray imaging, because the two masks remain in place when the flat fields are acquired. That is, the masks influence the intensity measured in the flat fields. In EI-XPCI there are two ways to perform a flat field correction. One can divide the projections by their corresponding flat fields, subsequently rescaling them by multiplication of the normalized projections with the mean intensity of the corresponding flat field. Another way is to process the projections and flat fields separately and compare them pixel-by-pixel as in [5].

In this paper, the influence of the masks on the intensity of flat fields is investigated. The effect of mask thickness on image quality was already shortly discussed in [6], where it was mentioned that thick masks may impose angular limitations on the beam. In our work, the mask thickness effect will be quantitatively studied. Using geometric ray optics, a model for the intensity profile is derived to study two theoretically expected influences on the flat fields. The derived theoretical results are validated using computer simulations in GATE, a GEANT4 application for tomographic emission experiments [7, 8].

## 2. METHODS

### 2.1. Edge illumination

The key components of an EI-XPCI setup are two masks with parallel aperture slits to achieve sensitivity for the refraction of the X-rays [6]: a sample mask and a detector mask, shown in Fig. 1. The sample mask is placed just in front of the sample and shapes the incoming X-ray cone beam into a number of separate smaller beamlets. The period of the sample mask is large enough to avoid interference of the beamlets. When interacting with the sample, the beamlets undergo attenuation, refraction, and scattering (broadening). The detector mask is placed just in front of the detector and covers the edges of the pixel columns (y-direction in Fig. 1), so the vertical aperture slits of the mask leave the middle section of the pixel exposed. Each beamlet strikes an aperture edge, partially illuminating each pixel.

When a beamlet is refracted by the sample, its position on the detector will shift. Depending on the direction of the shift, towards or away from the aperture, an intensity increase or decrease is measured, respectively. However, attenuation will also cause a decrease in measured intensity. To untangle the information of attenuation, refraction and scattering, an illumination curve is measured, which represents the measured intensity of a certain pixel as a function of the displacement of the sample mask. The illumination curve is sampled by acquiring flat fields for different positions of the sample mask, after which a Gaussian function is fitted to the sampled points. Subsequently, this procedure is repeated with the sample inserted in the beam, directly behind the sample mask. The attenuation contrast is retrieved by quantifying the change in surface under the Gaussian function, while the shift of the Gaussian relates to the refraction an-

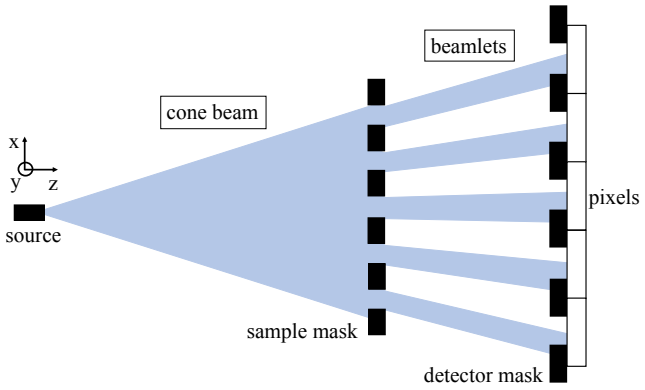


**Fig. 1**. The basic edge illumination set-up, not drawn to scale.

gle and the broadening to the amount of scatter. A retrieval algorithm is given in more detail in [3].

### 2.2. A model for the flat field intensity

The intensity profile of the flat field can be derived from a model based on geometric ray optics. In the model, the sample mask is aligned with the detector mask, so that each beamlet hits the middle of its pixel column. This position corresponds to the top of the illumination curve. The absorption of the sample mask is included in the model. Assuming a perfectly absorbing mask, the corresponding relative intensity decrease is denoted by $\kappa$ and can be calculated using the period $P$ and the aperture width $a$ of the sample mask:

$$\kappa = \frac{P-a}{P}. \tag{1}$$

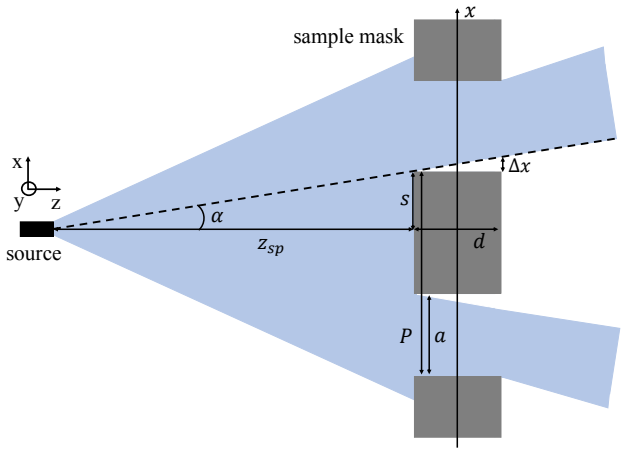


**Fig. 2**. Illustration of the shadow effect for the sample mask, not drawn to scale.

A first mask influence is here referred to as the *shadow effect* and is derived using Fig. 2. When the X-rays hit the edge of the sample mask under an angle $\alpha$, a shadow of width $\Delta x$ is created. The length $\Delta x$ is equal to $d \tan\alpha$, with $d$ the thickness of the sample mask and $\tan\alpha = s/z_{sp}$, with $z_{sp}$ the distance between the source and the sample mask. The variable distance $s$ is given by $s = |x| - a/2$, with $x$ the discrete positions of the middle of the apertures along the $x$-direction. The relative intensity decrease caused by the shadow effect is denoted by $\xi$ and given by the ratio of $\Delta x$ to the aperture width $a$. Hence, $\xi$ is given by:

$$\xi = \frac{\Delta x}{a} = \frac{(|x| - \frac{a}{2})d}{a z_{sp}}. \tag{2}$$

A second mask influence on the measured intensity, which we refer to as the *crown effect*, is caused by total external reflection of the X-rays at the surface of the mask, which occurs because the real part of the refractive index $n$ of a material is smaller than 1 for X-rays [9]. This causes X-rays to refract away from the normal when passing from air to the mask. If the angle of incidence becomes larger than a critical angle $\theta_c$, the X-rays are totally reflected from the surface of the mask. The critical grazing angle is given by $\beta_c = 90° - \theta_c$. If the X-rays hit the mask under a grazing angle $\beta > \beta_c$, the X-rays refract into the mask and are absorbed. If $\beta < \beta_c$ the X-rays reflect from the surface of the mask towards the detector, causing an increase in measured intensity, which is derived using Fig. 3.

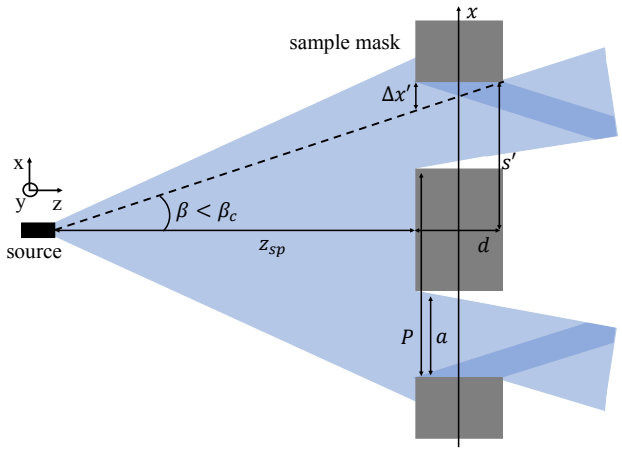


**Fig. 3**. Illustration of the crown effect for the sample mask, not drawn to scale. The totally reflected X-rays are shown in a darker color.

The X-rays that pass through the section $\Delta x'$ in Fig. 3 totally reflect from the surface of the mask towards the detector. The relative intensity increase caused by the crown effect is denoted by $\zeta$ and is given by the ratio of $\Delta x'$ to the aperture width $a$. The length $\Delta x'$ is equal to $d \tan\beta$, where $\tan\beta = s'/(z_{sp} + d)$ with $s'$ a variable distance given by $s' = |x| + a/2$ and $x$ the discrete positions of the middle of the apertures along the $x$-direction. However, the X-rays can only reflect if $\beta < \beta_c$. To know the position that lies at the boundary ($\beta = \beta_c$), a critical position $p$ is calculated as $p = (z_{sp} + d)\tan\beta_c$. With this position, a rectangular function $\Theta(x) = H(x + p) - H(x - p)$ is defined, with $H(x)$ the Heaviside step function. To apply the constraint on the reflection, the function $\Theta(x)$ is multiplied with the relative intensity increase:

$$\zeta = \frac{\Delta x'}{a} = \frac{(|x| + \frac{a}{2})d}{(z_{sp} + d)a}\Theta(x). \tag{3}$$

A theoretical intensity profile of the flat field can then be composed by combining Eqs. (1), (2) and (3):

$$I = I_0(1-\kappa)(1-\xi)(1+\zeta). \quad (4)$$

With $I_0$ the mean intensity of the flat field without the masks. However, Eq. (4) does not fully account for reflection at the sample mask, which changes the direction of the X-rays. That is, reflected X-rays are detected in a different pixel than expected, as illustrated in Fig. 4.

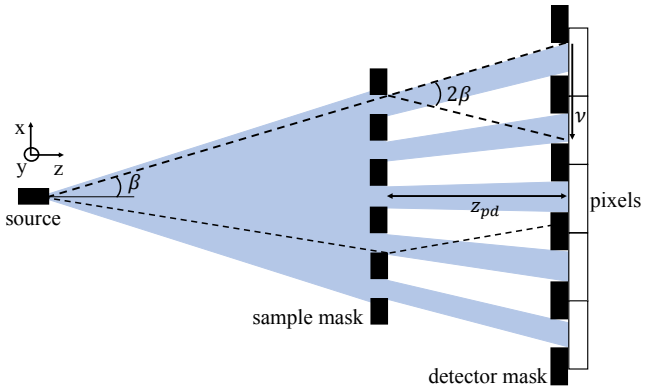


**Fig. 4**. An illustration of the shift $\nu$ caused by the reflection at the sample mask, not drawn to scale.

The reflection causes a shift of the X-rays on the detector, given by $\nu = -2z_{pd}\tan\beta$. The shift is negative for a positive $\beta$, implying a shift direction opposite to the x-direction. Firstly, the shift is used to determine whether the reflected X-rays hit the detector mask or not. This is done by calculating the position where they hit the detector and determining if this position is covered by the detector mask, using the known mask position. If the reflected X-rays hit the mask, they are assumed to be fully absorbed. This is implemented by setting the contribution to the intensity increase in $\zeta$ to zero, with $\zeta$ a vector, that contains in each element the relative intensity increase due to the crown effect for the corresponding aperture, as calculated by Eq. (3). Secondly, the actual shift of the X-rays is implemented by rebinning the values in $\zeta$, using an approximated shift $\nu'$. This shift $\nu'$ is expressed in an amount of pixels by dividing $|\nu|$ by the width of a pixel and then rounding it towards 0. This gave empirically the best approximation. Using $\nu'$, each element $(ii)$ of $\zeta$ is rebinned to a new element $(ii+\nu')$. It may happen that this causes multiple elements to be rebinned to the same element, causing an even larger intensity increase, however, the opposite also happens. The rebinned version of $\zeta$ is denoted as $\tau$, leading to the following approximated model for the intensity profile of the flat field:

$$I = I_0(1-\kappa)(1-\xi)(1+\tau) \quad . \quad (5)$$

### 2.3. Edge Illumination in GATE

The derived model was experimentally validated using computer simulations in GATE, augmented with tools for phase contrast imaging [10, 11]. Using Monte Carlo methods, GATE simulates a number of photons that interact with the defined environment through physical processes. The X-ray source is a square with a surface area of $0.1\,\mu m \times 0.1\,\mu m$ and produces a monochromatic X-ray cone beam (25 keV, $1.22^\circ$ opening angle) that traverses air ($n = 1$). The detector is a grid of $300 \times 300$ silicon pixels, each with an area of $100\,\mu m \times 100\,\mu m$ and a thickness of $3\,mm$. The detector is positioned $2.0\,m$ away from the source. The detector mask is placed right in front of the detector and has a thickness of $150\,\mu m$, an aperture width of $40\,\mu m$ and a period of $100\,\mu m$, equal to the width of a pixel. The sample mask is placed at $1.6\,m$ from the source and has a thickness $d = 150\,\mu m$ ($z_{sp} = 1.6\,m - d/2$), an aperture width $a = 32.03\,\mu m$ and a period $P = 80.06\,\mu m$. The sample mask is aligned with the detector mask, such that the beamlets hit the middle of each pixel column and have a width equal to the aperture width of the detector mask. Both masks are made of gold with a density of $19.3\,g/cm^3$. The real part of the complex refractive index of the gold is given by $n = 1-\delta$, with $\delta = 5.12 \cdot 10^{-6}$ [12]. For each simulation, $10^9$ photons are generated by the source. The output of each simulation is the flat field measured by the detector, from which an intensity profile is then calculated by taking the mean intensity of each column (y-direction in Fig. 1).

## 3. RESULTS & DISCUSSION

Fig. 5 shows the simulated mean intensity profile of the flat field from the simulation with both masks added to the experimental setup. The simulated profile is compared to the approximated profile from Eq. (5). As can be observed from Fig. 5, the theoretically derived intensity profile has a strong resemblance with the measured intensity profile.

In Fig. 5, a decrease in intensity towards the edges of the detector is observed that is much larger than predicted by the inverse square law. The observed decrease is caused by Compton- and Rayleigh scattering of the X-rays in the edges of the detector. If the scattering occurs in the middle of the detector, the X-rays scatter to neighboring pixels. However, if the scattering occurs in the edges it becomes more likely for the X-rays to exit the detector before detection. An extensive study of this scattering is beyond the scope of this paper, but an additional simulation was performed where the scattering was disabled to support this claim. The result is displayed in Fig. 6, where it can be observed that with scattering disabled, no intensity decrease towards the edges of the detector occurs.

It may prove useful to also conduct physical experiments to compare the results. In the computer simulations, the masks had a perfect geometry with smooth surfaces and sharp edges. In a physical experiment, however, it is likely that the masks have defects, rough surfaces and some other irregularities [13]. It is expected that these imperfections will result in a blurred crown effect, compared to the theoretically derived crown effect.

## 4. CONCLUSIONS

In this paper, theoretical flat field profiles of EI-XPCI setups have been derived, where influences of the masks were studied. A model for the intensity profile of the flat field was derived using geometric ray optics. This model describes two important influences of the masks on the intensity of the flat field: the shadow effect and the crown effect. The shadow effect causes an intensity decrease because of a shadow thrown by the mask on the detector. The crown effect causes an intensity increase because of total external reflection of the X-rays from the mask surface: instead of being absorbed by the mask, the X-rays are reflected towards the detector. The theoretical model was experimentally validated with Monte Carlo simulations using GATE. A strong resemblance was observed between the theoretical model and the experimental results.

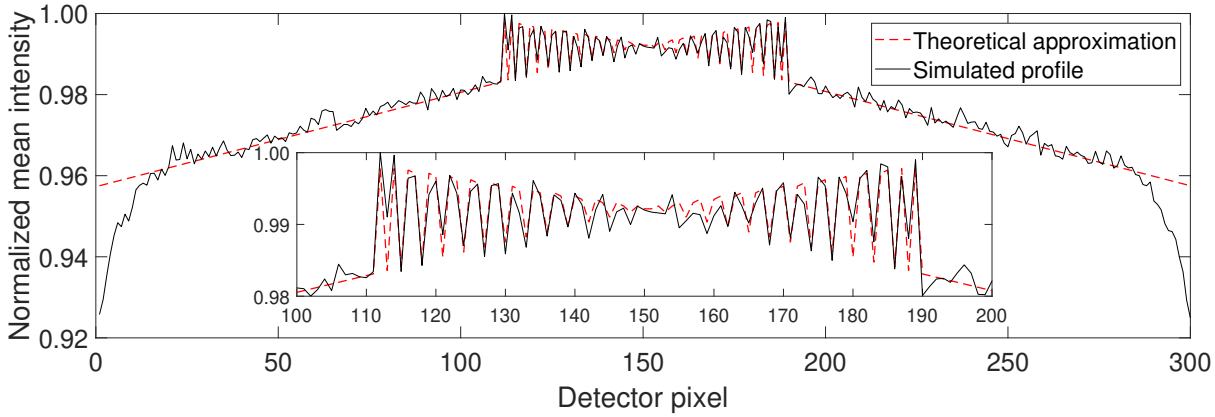


**Fig. 5**. The normalized mean intensity profile of the flatfield from the simulation with both masks, compared to the approximated intensity profile from Eq. (5). The area of the crown effect is enlarged to provide a better comparison.

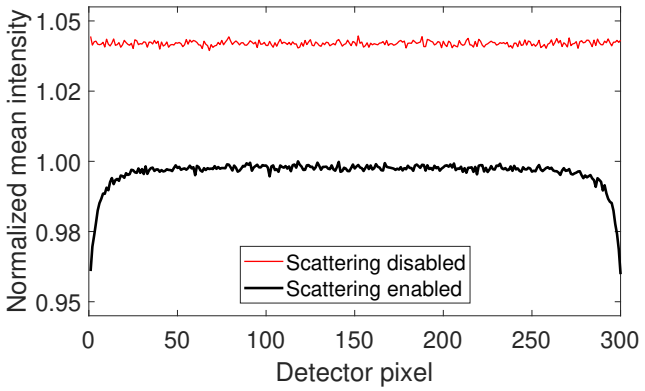


**Fig. 6**. The normalized mean intensity profile of the flat field in the simulation without any masks. A comparison is made between a simulation where Rayleigh- and Compton-scattering is enabled and one where the scattering is disabled.

## 5. COMPLIANCE WITH ETHICAL STANDARDS

This is a numerical simulation study for which no ethical approval was required.

## 6. ACKNOWLEDGMENTS

The research was supported by the Research Foundation - Flanders (FWO) (G090020N, G094320N, S003421N, 11D8319N) and EU Interreg Flanders-Netherlands Smart*Light (0386).

## 7. REFERENCES

[1] A. Momose, "Recent advances in X-ray phase imaging," *Japanese Journal of Applied Physics*, vol. 44, pp. 6355–6367, Sept. 2005.

[2] M. Endrizzi, "X-ray phase-contrast imaging," *Nuclear Instruments and Methods in Physics Research A*, vol. 878, pp. 88–98, Jan. 2018.

[3] M. Endrizzi and A. Olivo, "Absorption, refraction and scattering retrieval with an edge-illumination-based imaging setup," *Journal of Physics D: Applied Physics*, vol. 47, pp. 505102, Nov. 2014.

[4] C. Jailin et al., "On the use of flat-fields for tomographic reconstruction," *Journal of Synchrotron Radiation*, vol. 24, pp. 220–231, Jan. 2017.

[5] M. Endrizzi et al., "Laboratory-based X-ray phase-contrast imaging with misaligned optical elements," *Applied Physics Letters*, vol. 107, pp. 124103, Sept. 2015.

[6] A. Olivo and R. Speller, "Modelling of a novel X-ray phase contrast imaging technique based on coded apertures," *Physics in Medicine and Biology*, vol. 52, pp. 6555–6573, Oct. 2007.

[7] G. Santin et al., "GATE: A geant4-based simulation platform for PET and SPECT integrating movement and time management," *IEEE Transactions on Nuclear Science*, vol. 50, pp. 1516–1521, Oct. 2003.

[8] S. Jan et al., "GATE: a simulation toolkit for PET and SPECT," *Physics in Medicine and Biology*, vol. 49, pp. 4543–4561, Sept. 2004.

[9] J. Als-Nielsen and D. McMorrow, *Elements of Modern X-ray Physics*, Wiley, 2 edition, 2011.

[10] J. Sanctorum, J. De Beenhouwer, and J. Sijbers, "X-ray phase-contrast simulations of fibrous phantoms using GATE," in *2018 IEEE Nuclear Science Symposium and Medical Imaging Conference Proceedings*. IEEE, 2018, pp. 1–5.

[11] J. Sanctorum, J. De Beenhouwer, and J. Sijbers, "X-ray phase contrast simulation for grating-based interferometry using GATE," *Optics Express*, vol. 28, no. 22, pp. 33390–33412, Oct. 2020.

[12] E. Gullikson, "X-ray interactions with matter," [Online]. Available: `http://henke.lbl.gov/optical_constants/`, 2010, Date last accessed 19-August-2020.

[13] S. Saghamanesh et al., "Edge-illumination X-ray phase contrast imaging with Pt-based metallic glass masks," *The Review of Scientific Instruments*, vol. 88, pp. 063705, June 2017.